Turbulent heat transfer in spacer-filled channels: experimental and computational study and selection of turbulence models

Michele Ciofalo*, Massimiliano Di Liberto, Mariagiorgia La Cerva, Alessandro Tamburini

Dipartimento di Ingegneria, Università degli Studi di Palermo, Viale delle Scienze ed. 6, 90128 Palermo, Italy

ABSTRACT

Heat transfer in spacer-filled channels of the kind used in Membrane Distillation was studied in the Reynolds number range 100-2000, encompassing both steady laminar and early-turbulent flow conditions. Experimental data, including distributions of the local heat transfer coefficient *h*, were obtained by Liquid Crystal Thermography and Digital Image Processing. Alternative turbulence models, both of first order (*k*-ε, RNG *k*-ε, *k*-ω, BSL *k*-ω, SST *k*-ω) and of second order (LRR RS, SSG RS, ωRS, BSL RS), were tested for their ability to predict measured distributions and mean values of *h*. The best agreement with the experimental results was provided by first-order ω-based models able to resolve the viscous/conductive sublayer, while all other models, and particularly ε-based models using wall functions, yielded disappointing predictions.

KEYWORDS

Membrane Distillation; Overlapped Spacer; Liquid Crystal Thermography; Computational Fluid Dynamics; RANS Turbulence Model; Heat Transfer

Declarations of interest: none

*Corresponding author – email: michele.ciofalo@unipa.it

1. Heat and mass transfer in spacer-filled channels

Membrane processes offer examples of heat or mass transfer in plane channels bearing mixing promoters of more or less tortuous geometry, aimed at reducing temperature or concentration polarization phenomena thus improving the process performance [1, 2]. Promoters usually consist of polymeric wires, or filaments, and play also the role of spacers, keeping a fixed distance between the opposite channel walls (membranes). For example, for a channel provided with an overlapped-wire spacer, figure 1 shows (a) a photograph of the spacer, and (b) the unit cell used as the computational domain.

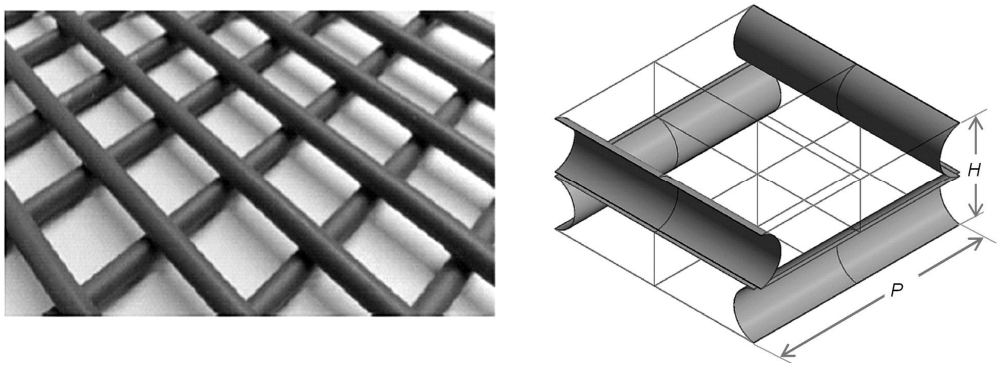

(a) (b)

Figure 1. Channel provided with an overlapped-wire spacer. (a) Photograph of the spacer; (b) unit cell (computational domain).

The nature of the main transfer phenomena involved (e.g. heat and/or mass transfer) and the flow conditions (e.g. laminar or turbulent) depend on the application considered. For example, in Electrodialysis [1] the channels are usually 0.1-1 mm thick, velocities range between 1 and a few cm/s, and thus the Reynolds number rarely exceeds 100, yielding steady laminar flow; the main process occurring in the fluid channels is the transfer of salt ions to or from the bounding membranes, giving rise to concentration polarization. On the other hand, in Membrane Distillation [2], feedwater channels are usually thicker (3-4 mm) and velocities may exceed 0.2 m/s, so that the Reynolds number may range up to ~2000 yielding (in the tortuous geometry created by the spacers) turbulent flow conditions. The transfer processes include heat transfer from the bulk fluid to the semi-permeable membrane walls, causing temperature polarization, and mass transfer of water vapor (accompanied by conductive transfer of sensible heat) through the membranes.

CFD simulations of spacer-filled channels for membrane processes started to appear in

the literature around the year 2000 and have been presented at an increasing rate since then. With specific reference to Membrane Distillation, Hitsov *et al.* [3], Fimbres-Wehis and Wiley [4], Karabelas *et al.* [5] and La Cerva *et al.* [6] presented reviews addressing a number of modelling issues.

2. Spacer configurations investigated and main definitions

The spacer geometry considered in the present study is sketched in figure 1. It consists of two overlapped layers of cylindrical rods arranged at 90°, with a pitch-to-channel height ratio P/H=2. Both in the experiments and in the numerical simulations, heat transfer occurred only from the top wall, representing the fluid-membrane interface, while the opposite bottom wall was adiabatic.

The flow attack angle θ may significantly affect flow and heat transfer [7–9]. Three values of θ were considered here: 0°, 45° and 90°. For θ = 0°, the flow is parallel to the layer of rods touching the top wall, where heat transfer occurs; for θ = 90° the flow is orthogonal to this top layer; for θ = 45° it bisects the angle formed by the two rod layers. The orientations at 0° and 90° are equivalent hydrodynamically (thus yielding the same friction coefficient), but not thermally due to the different flow/spacer rods relative orientation in the proximity of the thermally active wall.

In order to define dimensionless quantities, reference was made to the corresponding "void" configuration, i.e. to a spacerless, laterally indefinite, plane channel of height H and hydraulic diameter $2H$. Thus, the definition of the bulk Reynolds number was

$$\mathrm{Re} = \frac{U \cdot 2H}{\nu} = \frac{2Q}{W \cdot \nu} \tag{1}$$

where $U = Q/(WH)$ is the mean "void channel" streamwise velocity (superficial velocity), Q the volume flow rate and W the channel's lateral dimension. This definition of Re is preferable to one based, for each specific geometry, on the actual hydraulic diameter and mean velocity (interstitial velocity), because it better highlights the influence of a given spacer configuration [6, 10].

3. Experimental technique, uncertainty analysis and typical results

The measurement of wall temperatures was performed by Thermochromic Liquid Crystals (TLC). Their use is well documented in the scientific literature both for the measurement of

surface temperature distributions [11, 12, 13] or for the joint visualization of flow and temperature fields [14, 15]. Details of the test section and of the image processing procedure were described in previous papers [10, 16], and only a short description of the experimental method will be provided here.

The test section, figure 2, consisted of a hot and a cold channel whose outer walls were 20 mm thick Plexiglas® slabs, separated by a 1 mm thick transparent polycarbonate (PC) layer. Hot water was forced to flow through one of the channels, filled with the spacer to be tested whose thickness established the channel height *H*. A sheet of Hallcrest® thermochromic liquid crystals, ~0.12 mm thick, was interposed between the spacer and the polycarbonate layer, with its visible surface touching this latter; a very thin layer of transparent silicone grease was used to provide adhesion and thermal contact between the TLC sheet and the PC layer. Cold water was forced in parallel flow on the opposite side of the polycarbonate layer, i.e. within the cold channel, which was left void (i.e., without a spacer) and whose height was 3 mm.

For the reasons explained in previous work [10] (see "supplementary material" section therein), experimental tests were carried out in a scaled-up spacer-channel configuration characterized by *H*=1 cm, *P*=2 cm.

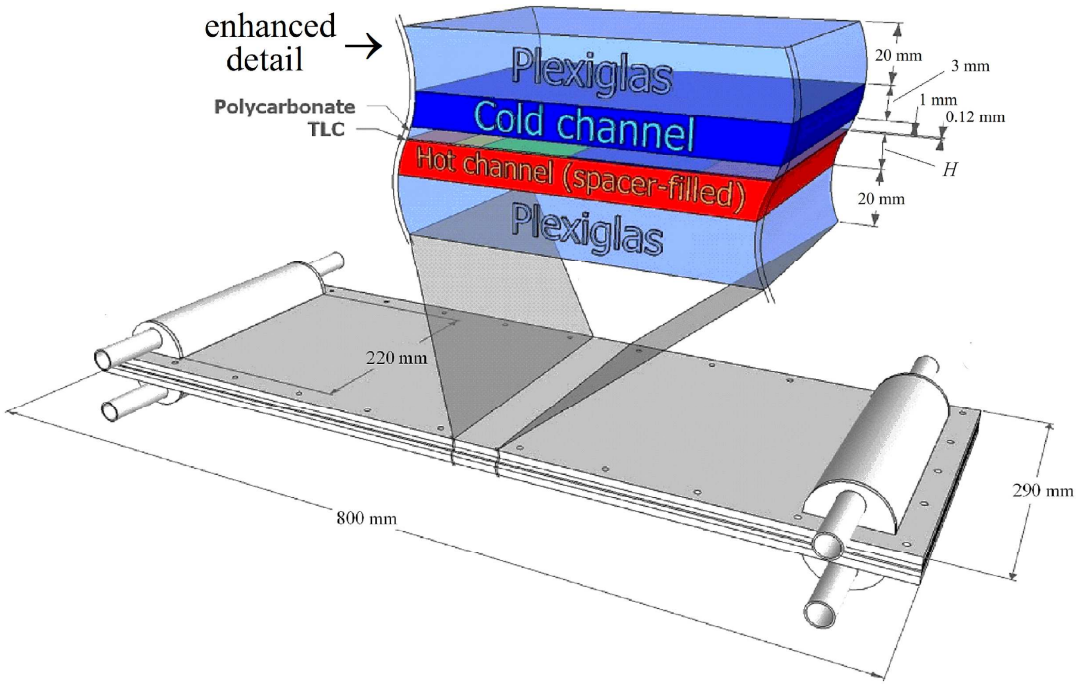

Figure 2. Representation of the test section with an enhanced detail of the different layers

The TLC colour distribution was recorded by a digital camera through the outer wall of the cold channel, the cold water, the polycarbonate layer, and the transparent polyester foil which makes up most of the TLC sheet's thickness. Images, acquired in RAW format, were converted into TIFF and then split into HSV (Hue, Saturation, Value) components. Only the Hue component was used to extract the temperature distribution.

The thermochromic response of the TLC sheet was characterized by an *in-situ* calibration, performed by the isothermal method [10, 16]. A 6th degree polynomial was employed to fit the data within the experimentally investigated range.

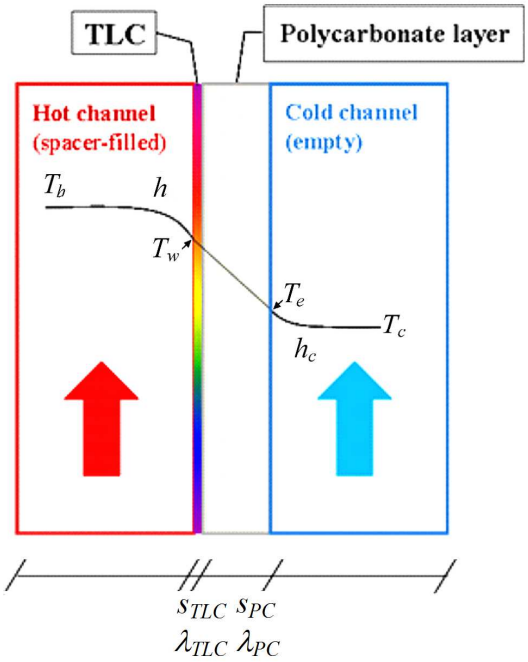

Figure 3. Sketch of the temperature profile across the test section.

The temperature profile across the different layers of the test section is schematically shown in figure 3. With reference to this sketch, an analysis of the heat transfer process under the assumption of one-dimensional transport gives the local hot-side heat transfer coefficient h as a function of the locally measured temperature T_w of the TLC sheet once the bulk temperatures T_b, T_c of the hot and cold fluids and the cold-side heat transfer coefficient h_c are known:

$$h = \frac{1}{r} \cdot \frac{T_w - T_c}{T_b - T_w} \tag{2}$$

in which r is an overall thermal resistance made up of the conductive thermal resistances s/λ of the thermochromic liquid crystal film (*TLC*) and of the polycarbonate layer (*PC*), in series with the convective thermal resistance $1/h_c$ associated with the cold channel:

$$r = \frac{s_{TLC}}{\lambda_{TLC}} + \frac{s_{PC}}{\lambda_{PC}} + \frac{1}{h_c} \tag{3}$$

T_b and T_c were measured by Pt100 RTDs at the inlet and outlet of the hot and cold channels and a linear variation of these quantities along the flow direction was assumed. The coefficient h_c was estimated by the Dittus-Bölter correlation ($\mathrm{Nu}=0.023\ \mathrm{Re}^{0.8}\ \mathrm{Pr}^{0.4}$) written for turbulent flow in the cold channel.

Liquid Crystal Thermography is mainly a whole-field temperature visualization technique; however, in several previous papers [10-12, 16] we have shown that, if properly calibrated and correctly applied, it can also provide quantitative measurements of heat transfer coefficients. Of course, a careful uncertainty analysis is necessary because the accuracy of experimental h values can affect the choice of turbulence models and wall functions [17].

According to Eqs. (2)-(3), h depends upon n=8 different measured or estimated quantities "x_i" corresponding to T_w, T_c, T_b, s_{TLC}, λ_{TLC}, s_{PC}, λ_{PC}, h_c. The relative uncertainty on h arising from the uncertainty on a generic x_i depends both on the uncertainty on x_i and on the sensitivity of h to x_i. This latter quantity is best characterized in dimensionless form by the sensitivity coefficient

$$S(h:x_i) = \frac{x_i}{h}\frac{\partial h}{\partial x_i} \tag{4}$$

which expresses the relative uncertainty on h caused by a unitary relative uncertainty on x_i.

In the following, the attention will be focussed on a specific test case characterized by a flow rate of 199 L/h (yielding Re≈690), θ=45°. Most of the conclusions, however, apply to other experimental conditions. For this case, figure 4(a) reports the instantaneous spatial distribution of the wall temperature T_w in a unit cell like that in figure 1(b). Figure 4(b) reports the corresponding distribution of the hot-side heat transfer coefficient h, derived from T_w using Eqs. (2)-(3). Table 1 summarizes the nominal value or range of each individual measured quantities x_i, the corresponding uncertainty σ_i, the formal expression of the sensitivity coefficient $S(h/\ x_i)$ and its value or range.

Table 1. Parameters for sensitivity analysis (Re=690, θ=45°)

Quantity x_i	Nominal value	Uncertainty	Sensitivity coefficient (expression)	Sensitivity coefficient (value or range)
T_w (wall)	2-D map (Fig.4.a)	0.2 [K]	$\frac{T_w(T_b-T_c)}{(T_b-T_w)(T_w-T_c)}$	2-D map (Fig.4.c)
T_c (cold bulk)	294.25 [K]	0.1 [K]	$-\frac{T_c}{T_w-T_c}$	2-D map (Fig.4.d)
T_b (hot bulk)	313.02 [K]	0.1 [K]	$-\frac{T_b}{T_b-T_w}$	2-D map (Fig.4.e)
s_{PC} (PC sheet)	1×10^{-3} [m]	0.5×10^{-4} [m]	$-\frac{1}{r}\frac{s_{PC}}{\lambda_{PC}}$	-0.802
λ_{PC} (PC sheet)	0.19 [$Wm^{-1}K^{-1}$]	0.02 [$Wm^{-1}K^{-1}$]	$\frac{1}{r}\frac{s_{PC}}{\lambda_{PC}}$	0.802
s_{TLC} (TLC sheet)	1.2×10^{-4} [m]	0.2×10^{-4} [m]	$-\frac{1}{r}\frac{s_{TLC}}{\lambda_{TLC}}$	-0.122
λ_{TLC} (TLC sheet)	0.15 [$Wm^{-1}K^{-1}$]	0.02 [$Wm^{-1}K^{-1}$]	$\frac{1}{r}\frac{s_{TLC}}{\lambda_{TLC}}$	0.122
h_c (cold side)	2000 [$Wm^{-2}K^{-1}$]	200 [$Wm^{-2}K^{-1}$]	$\frac{1}{rh_c}$	0.076

For example, the negative value of about -0.8 reported for $S(h:s_{PC})$ means that a 5% overestimation of the polycarbonate sheet thickness s_{PC} results in a ~4% underestimation of h.

With respect to the quantities T_w, T_c and T_b, the sensitivity coefficient is a function of place. The relevant maps in a unit cell of the spacer lattice are reported in figures 4(c)-4(e).

The sensitivity coefficients with respect to the wall temperature, $S(h:T_w)$ and to the hot bulk temperature, $S(h:T_b)$, see figures 4(c) and 4(e), are of comparable entity, although of opposite sign. They are large (~10^2), implying that a 1% uncertainty on T_w or T_b would result in a 100% uncertainty on h; however, the actual relative uncertainty on either of the above temperatures is much smaller, <10^{-3} (0.2/300, see Table 1), so that the corresponding uncertainty on h does not exceed a few percent. The sensitivity to the cold bulk temperature, figure 4(d), is lower (order 10^1), implying that an accurate assessment of T_c is not necessary.

Finally, the overall relative uncertainty of h can be estimated as [18]:

$$\frac{\sigma_h}{h}=\sqrt{\sum_{i=1}^{n}\left[S(h:x_i)\right]^2\left[\frac{\sigma_i}{x_i}\right]^2} \tag{5}$$

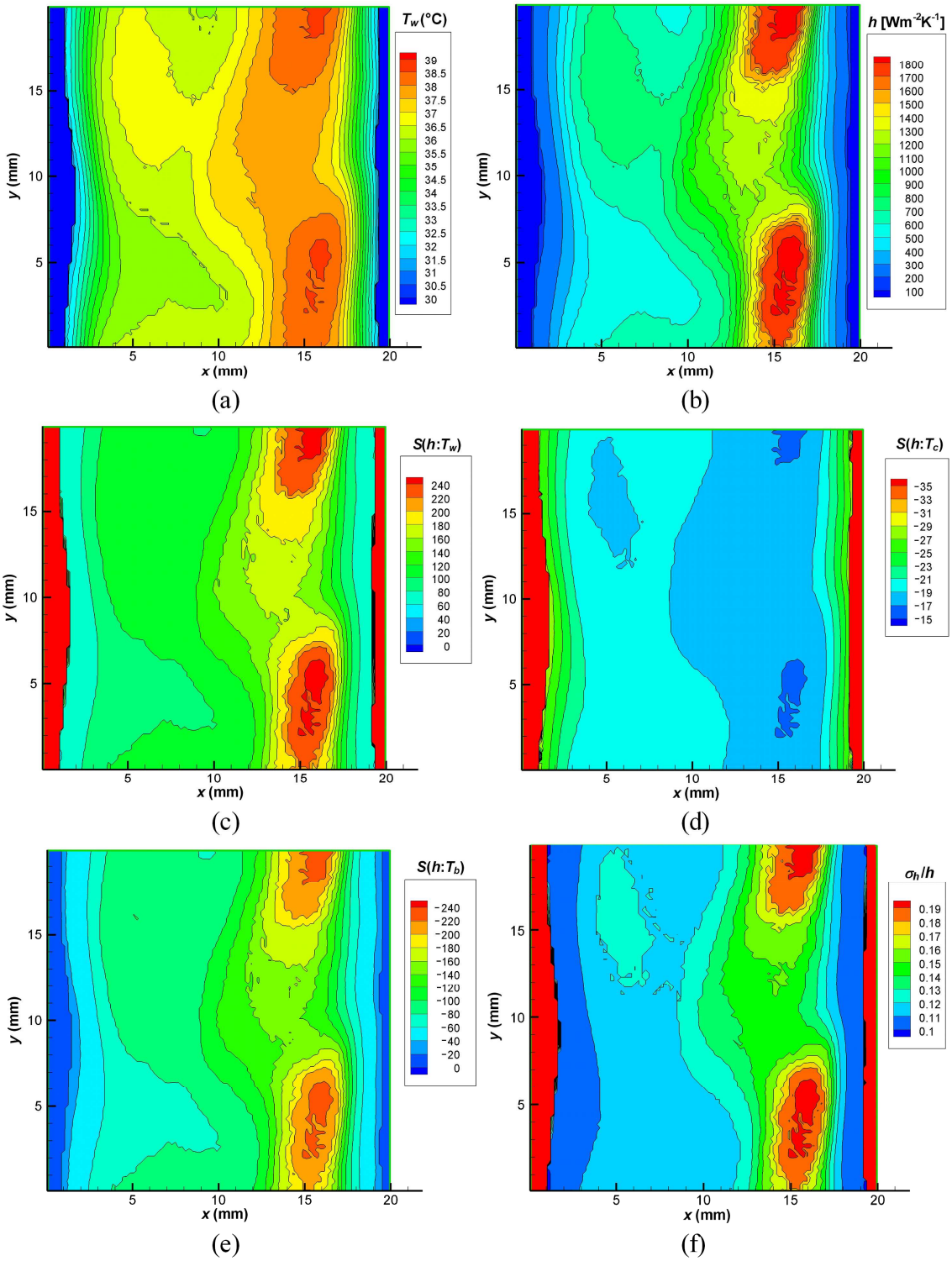

Figure 4. Case θ=45°, Re=690: (a) wall temperature; (b) local heat transfer coefficient h; (c) sensitivity coefficient $S(h{:}T_w)$; (d) sensitivity coefficient $S(h{:}T_c)$; (e) sensitivity coefficient $S(h{:}T_b)$; (f) overall relative uncertainty on h. Flow is from top left to bottom right.

The resulting distribution of σ_h/h, based on the relative uncertainties and sensitivity coefficients in Table 1 and figure 4(c)-4(e), is shown in Figure 4(f). This quantity varies between ~10% and ~15% over most of the unit cell, with higher values (up to ~20%) only in correspondence with h maxima. An approximately linear correlation exists between the relative uncertainty σ_h/h and the value of h. A large relative uncertainty exists also in the areas where the active wall touches the spacers (vertical side bands in figure 4), but here h is very low so that the absolute uncertainty on h is negligible.

Although a relative uncertainty of 10 to 20% may look large, the advantage of a high spatial resolution, whole-field assessment of h is priceless, especially if the influence of the spacer geometry and flow attack angle have to be investigated with a view to develop higher-performance spacers. Also for the validation of computational results and turbulence models, the knowledge of the spatial distribution of the heat transfer coefficient may be as valuable as the accurate knowledge of its mean or pointwise values.

The uncertainty on the Reynolds number, Eq. (1), is negligible because the flow rate Q was measured by a high accuracy magnetic flowmeter, previously calibrated by direct volume measurements, while the width W of the channel was exactly known.

For overlapped spacers with P/H=2, experimental results were obtained in the Reynolds number range 100~2000. The visual observation of the test section showed that the alternate pattern of hot and cold wall regions (as indicated by the TLC colour) remained steady only up to Re≈400. At higher Reynolds numbers, the TLC colour pattern exhibited time-dependent irregular oscillations with small amplitude and characteristic frequencies of a few Hz. Note that neither the amplitude nor the frequency of these irregularities are immediately related with the amplitude and frequency of turbulent temperature fluctuations proper, because of the damping role played by the thermal inertia of the TLC foil itself and of the polycarbonate sheet immediately in contact with it.

In previous work [10], the individual temperature distributions taken at a generic instant for 28 unit cells of the type shown in figure 1(b) were preliminary averaged to yield ensemble-averaged distributions, from which the heat transfer coefficient h was extracted. Such ensemble-averaged distributions pertaining to different instants were found to be practically identical. In this work, it was preferred to process the images of a single unit cell, time-averaging the wall temperature distributions pertaining to 10 instants taken at intervals of about 10 s, long enough for the correlations between individual distributions to vanish.

Results were found to be practically indistinguishable from those obtained by ensemble-averaging as explained above. Note that averaging will reduce the uncertainties discussed above, although a precise estimate of this reduction would require a knowledge of the relative contribution of random and systematic errors to the overall uncertainty.

Figure 5 reports experimental time-averaged distributions of the local heat transfer coefficient h on the top (thermally active) wall for the three orientations θ=0° (a), 45° (b) and 90° (c) and for moderate Reynolds numbers, ranging between ~600 and ~750. To the right of each graph the Reynolds number Re, the surface-averaged value of h, $\langle h \rangle$, and the flow direction are shown. For readability, two different colour scales are used, one for θ=0° and one for θ=45° and 90°. Figure 5(b) is essentially a time-averaged version of figure 4(b).

The orientation θ=0° (a) yields the most uniform distribution of h but rather low values of this quantity. The orientation θ=90° (c) yields high values of h immediately upstream of each transverse rod, but low values downstream, and a surface-averaged value of h which is only slightly higher than that obtained for 0° (if the difference in Reynolds number is taken into account). The orientation θ=45° (b) provides the highest average h and a forward-skewed distribution similar to that observed for θ=90°.

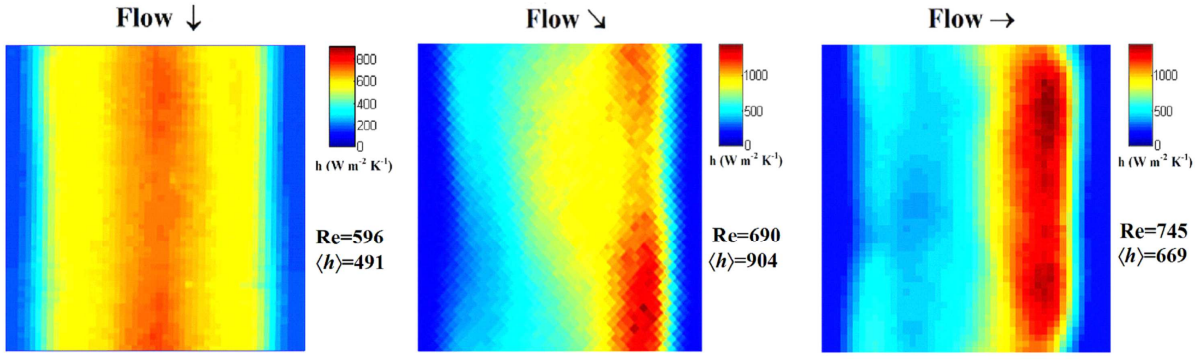

(a) (b) (c)

Figure 5. Experimental distribution of the local heat transfer coefficient h on the top (thermally active) wall for Re≈600-750 and different flow attack angles. (a) θ=0°, Re=596; (b) θ=45°, Re=690; (c) θ=90°, Re=745. The direction of the flow and the surface-averaged values of h, $\langle h \rangle$, are reported.

Figure 6 reports corresponding distributions obtained for high Re (1820-1850). As in the lower Re cases, different colour scales are used. Remarks similar to the above ones apply. The highest values of $\langle h \rangle$ are still provided by the orientation θ=45° (b). The orientation θ=90° (c) yields a marked spanwise non-uniformity in the distribution of h, with a relative minimum at the center of the region located immediately upstream of the transverse rod.

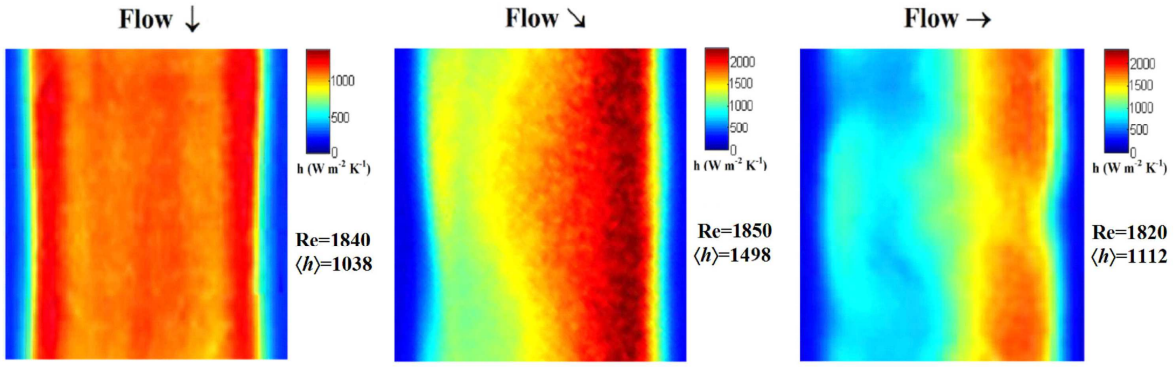

(a) (b) (c)

Figure 6. Experimental distribution of the local heat transfer coefficient h on the top (thermally active) wall for Re≈1820-1850 and different flow attack angles. (a) θ=0°, Re=1840; (b) θ=45°, Re=1850; (c) θ=90°, Re=1820. The direction of the flow and the surface-averaged values of h, $\langle h \rangle$, are reported.

Experimental results for the surface-averaged heat transfer coefficient are summarized in Table 2 as functions of Re for all three orientations. Bold characters denote the selected test cases in figures 5 and 6, for which detailed CFD results will be shown in Section 5.

Table 2. Experimental values of the surface-averaged heat transfer coefficient $\langle h \rangle$ on the top (thermally active) wall for Re≈100-2000 and different flow attack angles.

θ=0°		**θ=45°**		**θ=90°**	
Re	$\langle h \rangle$	Re	$\langle h \rangle$	Re	$\langle h \rangle$
136	293	135	245	141	221
210	299	291	377	214	276
356	304	407	532	341	314
498	405	540	732	414	366
596	**491**	**690**	**904**	482	415
688	581	928	1108	562	486
797	666	1220	1271	667	586
946	765	1526	1404	**745**	**669**
1045	816	**1850**	**1498**	878	755
1212	882			973	817
1408	936			1054	875
1574	976			1170	928
1756	1020			1284	972
1840	**1038**			1388	999
				1495	1029
				1643	1070
				1730	1088
				1820	**1112**

4 Computational methods and turbulence models

In the present study, the computational domain was the unit cell in figure 1(b). Mathematically, the problem was described by the continuity, Navier-Stokes and energy equations for a constant-property fluid. The "unit cell" treatment discussed in [10] (see "supplementary material" section therein) allowed periodicity conditions to be imposed to all variables at the opposite faces of the computational domain.

No slip conditions (u_i=0) were imposed at the top and bottom walls and on the rods' surface. In regard to the thermal boundary conditions, the bottom wall and the rods were assumed to be adiabatic ($q"_w$=0), while at the top wall a third type (Robin) boundary condition was imposed:

$$T_w - T_c = r\, q"_w \tag{6}$$

mimicking the actual boundary condition holding in the experiments, and with the same values for the outer temperature T_c (19°C) and for the thermal resistance r (~$6.5 \cdot 10^{-3}$ m^2K/W).

In the simulations, a driving pressure gradient directed along the main flow direction (which depends on the flow attack angle θ) is imposed as a source term in the Navier-Stokes equations and the flow rate is computed as part of the solution. At each iteration of the numerical solver, the velocity component along the main flow direction is volume-averaged in the computational domain (unit cell) and is then multiplied by the porosity of the spacer (fluid volume/total volume) to obtain the superficial velocity U. The amplitude of the driving pressure gradient is dynamically adjusted so that U matches the experimental value.

The bulk temperature T_b is computed as the mass flow-weighted average of T on the inlet openings of the unit cell. The wall temperature T_w is directly provided by the CFX code as part of the solution. The wall heat flux $q"_w$ is also provided by the code, or can be computed from T_w using Eq.(6).

Also the spacer geometry was the same as the experimental one and the fluid was assumed to be water at 39°C with physical properties ρ=992.5 kg/m^3, c_p=4179 J/(kgK), λ=0.63 W/(mK), μ=6.67×10^{-4} Pa·s, yielding a Prandtl number of 4.42.

The computational tool used was the Ansys-CFX finite volume code, Releases 17 and 18 [19]. Following a careful grid dependence study, conducted by using the SST k-ω turbulence model, a very fine block-structured finite volume grid of 4.2 million cells, all hexahedral, was

chosen. The dimensionless distance y^+ of the first near-wall grid point (centre of a control volume) from the wall varied from ~1 to ~2 in the range of conditions investigated in the present study.

The turbulence models which were compared are summarized in Table 3, where they are grouped into four families according to two criteria. The former criterion distinguishes first order eddy viscosity / eddy diffusivity models (k-ε, RNG k-ε, k-ω, BSL k-ω, SST k-ω) from second order Reynolds stress / Reynolds flux models (LRR RS, SSG RS, ω RS, BSL RS). The latter criterion distinguishes ω-based models, in which the viscous / conductive sublayer is explicitly resolved by the computational grid (k-ω, BSL k-ω, SST k-ω, ω RS, BSL RS) from k-based models, in which the sublayer is not explicitly resolved and wall functions are used (k-ε, RNG k-ε, LRR RS, SSG RS). Note that the same computational grid, which does resolve the sublayer, is used in all cases, but the adoption of the "scalable wall functions" option in Ansys-CFX forces the program to ignore all control volumes placed inside the sublayer and to bridge the first volumes lying outside this region with wall values through the wall function approach.

Table 3. Turbulence models tested

	k-based (wall functions)	ω-based (no wall functions)
First order (eddy viscosity / diffusivity)	k-ε, RNG k-ε	k-ω, BSL k-ω, SST k-ω
Second order (Reynolds stress / flux)	LRR RS, SSG RS	ω RS, BSL RS

Space does not allow here a complete description of the governing equations characterizing all models. A brief description, which includes relevant references, can be given as follows.

- The k-ε model [20] solves two transport equations for the turbulence energy k and its dissipation rate ε; the turbulent viscosity is then obtained as $\mu_t=\rho C_\mu k^2/\varepsilon$. It is the industry standard model and is described in detail in all textbooks on turbulence.

- The RNG k-ε model is based on the renormalization group analysis of the Navier-Stokes equations [21]. The resulting transport equations for turbulence energy and dissipation resemble those in the standard k-ε model, but the model constants differ, and the constant $C_{\varepsilon 1}$ in the production term for ε becomes a function $C_{\varepsilon 1,\mathrm{RNG}}$ of k, ε, and the k-production term.

- The k-ω model [22] solves transport equations for the turbulence energy k and its relative

dissipation rate (turbulence frequency) $\omega=\varepsilon/k$. The turbulent viscosity is obtained as $\mu_t=\rho k/\omega$.

- The BSL (baseline) k-ω model [23] is a blending between the k-ω model near the walls and the k-ε model in the outer region. It was developed to overcome a well known problem presented by the k-ω model, i. e. a strong sensitivity to freestream conditions.

- The SST k-ω model [22, 24] differs from the BSL k-ω for the presence of a limiter to the eddy-viscosity, accounting for the transport of the turbulent shear stresses. It is believed to give highly accurate predictions of the onset and amount of flow separation under adverse pressure gradients and is currently adopted as default turbulence model in most CFD codes.

- ε-based Reynolds stress models do not use the eddy viscosity hypothesis, but solve transport equations for all six components of the Reynolds stress tensor, the dissipation rate ε, and the three components of the turbulent heat flux (if present). The two versions LRR RS, from Launder, Reece and Rodi [25], and SSG RS, from Speziale, Sarkar and Gatski [26], are similar to each other and differ only in the values of some of the model constants.

- ω-based Reynolds stress models differ from ε-based Reynolds stress models in that the transport equation for dissipation ε is replaced by one for the turbulence frequency ω. CFX [19] provides two variants, the ω RS and the BSL (baseline) RS models. The two models relate to each other in a similar way as the two equation k-ω and BSL k-ω models and are expected to provide similar results.

5 Comparative results

Tables 4 and 5 summarize experimental and computational results, respectively obtained for moderate Re (~600-750) and for high Re (~1820-1850). For each flow attack angle θ and Reynolds number Re, the surface-averaged wall heat transfer coefficient $\langle h \rangle$ is reported. Results will be discussed in detail in the following, focussing not only on average values but also on the corresponding spatial distributions of the local heat transfer coefficient h.

Table 4. Summary results for moderate Reynolds number

	θ=0° (Re=596)	θ=45° (Re=690)	θ=90° (Re=745)
	$\langle h \rangle$	$\langle h \rangle$	$\langle h \rangle$
EXP	**491**	**904**	**669**
k-ω	456	786	577
BSL k-ω	509	710	748
SST k-ω	487	779	695
ωRS	377	676	479
BSL RS	466	752	621
k-ε	604	613	627
RNG k-ε	616	600	713
LRR RS	694	544	730
SSG RS	653	543	730

Table 5. Summary results for high Reynolds number

	θ=0° (Re=1840)	θ=45° (Re=1850)	θ=90° (Re=1820)
	$\langle h \rangle$	$\langle h \rangle$	$\langle h \rangle$
EXP	**1038**	**1498**	**1112**
k-ω	1160	1354	1196
BSL k-ω	1189	1391	1343
SST k-ω	1142	1416	1219
ωRS	1228	1327	1137
BSL RS	1254	1298	1295
k-ε	1630	1201	1390
RNG k-ε	1674	1123	1414
LRR RS	1805	1068	1550
SSG RS	1818	1040	1428

The following figures 7 to 9 report the distributions of h on the top (thermally active) wall of the unit cell as predicted by all turbulence models for moderate Reynolds numbers (~600-750) and flow attack angles θ=0°, 45° and 90°, respectively. Surface averages $\langle h \rangle$ are also indicated. The corresponding experimental distributions, reported above in figure 5 (a-c), are replicated for comparison purposes in the last map.

For Re=596 and a flow attack angle θ=0°, figure 7, h exhibits an experimental surface-averaged value $\langle h \rangle$ of 491. Distributions and average values in good agreement with the experimental results are provided only by the eddy viscosity ω-based models (k-ω, BSL k-ω, SST k-ω). In particular, the closest average value is provided by the SST k-ω model. Second order ω-based models (ωRS, BSL RS) yield unphysical distributions of h, with

multiple maxima along the spanwise direction (horizontal in the figures). The ωRS model met also convergence difficulties, yielding oscillatory solutions and a heavy underprediction of $\langle h \rangle$. *k*-based models using wall functions, both of the first order (*k*-ε, RNG *k*-ε) and of the second order (LRR RS, SSG RS), yield flat distributions of *h*, with the absence of values below 3-400 $Wm^{-2}K^{-1}$, which made it advisable to use a different color key in the maps. These models yield also a heavy overprediction of $\langle h \rangle$ and unphysical distributions of *h*, exhibiting a strong asymmetry about the main flow direction.

It should be observed that, in the present simulations, for θ=0° and 90° symmetry of the computed flow and thermal fields about the main flow direction is expected as a consequence of the geometric symmetry (see figure 2), but is not explicitly enforced: in fact, the side boundaries are defined as periodicity planes and not as symmetry planes. Therefore, a simulation's ability to reproduce the expected solution symmetries is itself a bonus, independent of the quantitative agreement on *h* or other quantities. Of course, symmetry could be enforced by defining the side boundaries as symmetry, and not periodicity, planes, but a moment's reflection shows that this approach, besides being somewhat artificial, would not be applicable to flow attack angles other than 0° or 90°.

Figure 8 reports computed distributions of *h* on the top wall for Re=690 and a flow attack angle θ=45°. Surface averages $\langle h \rangle$ are also shown. The corresponding experimental distribution was reported in figure 5(b) and exhibits a surface-averaged value $\langle h \rangle$ of 904. In this case, *h* distributions in qualitative agreement with the experimental results are provided by all ω-based models (*k*-ω, BSL *k*-ω, SST *k*-ω, ωRS and BSL RS), which, however, all underpredict $\langle h \rangle$. The average value of $\langle h \rangle$ closest to the experimental one (786 against 904 $Wm^{-2}K^{-1}$) is provided by the *k*-ω model. All *k*-based models using wall functions, both of the first order (*k*-ε, RNG *k*-ε) and of the second order (LRR RS, SSG RS) yield (i) a very heavy underprediction of $\langle h \rangle$ and (ii), as in the case θ=0°, flat spatial distributions of *h*, in which both the highest and the lowest values are absent. Again, this made it advisable to use a different color key than for the ω-based models.

Finally, figure 9 reports computed distributions of *h* on the top wall for Re=745 and a flow attack angle θ=90°. Surface averages $\langle h \rangle$ are also shown. The corresponding experimental distribution was reported in figure 5(c) and exhibits a surface-averaged value $\langle h \rangle$ of 669. For this flow attack angle, *h* distributions in qualitative agreement with the

experimental results are provided by first-order ω-based models (k-ω, BSL k-ω, SST k-ω); the best agreement on $\langle h \rangle$ is provided by the SST k-ω model, which overpredicts it by ~4%. Second-order ω-based models (ω RS, BSL RS) yield excessively flat distributions of h and some unphysical asymmetry about the flow direction; the ω RS model, in particular, gives also a strong underprediction of $\langle h \rangle$. Note that, despite their similarity, the k-ω model underpredicts $\langle h \rangle$ by ~14% while the BSL k-ω model overpredicts it by ~12%. All k-based models using wall functions, both of the first order (k-ε, RNG k-ε) and of the second order (LRR RS, SSG RS), yield wrong spatial distributions of h, with excessively uniform values over the active wall and a strong unphysical asymmetry about the flow direction. Among them, the k-ε model underpredicts $\langle h \rangle$ by ~4% while all others (RNG k-ε, LRR RS, SSG RS) overpredict $\langle h \rangle$ by 7-9%.

In the light of the above results, it is clear that for Reynolds numbers between ~600 and ~750 acceptable predictions of the mean value and the overall distribution of the local heat transfer coefficient h can only be obtained by using ω-based models, which explicitly resolve the near-wall layer.

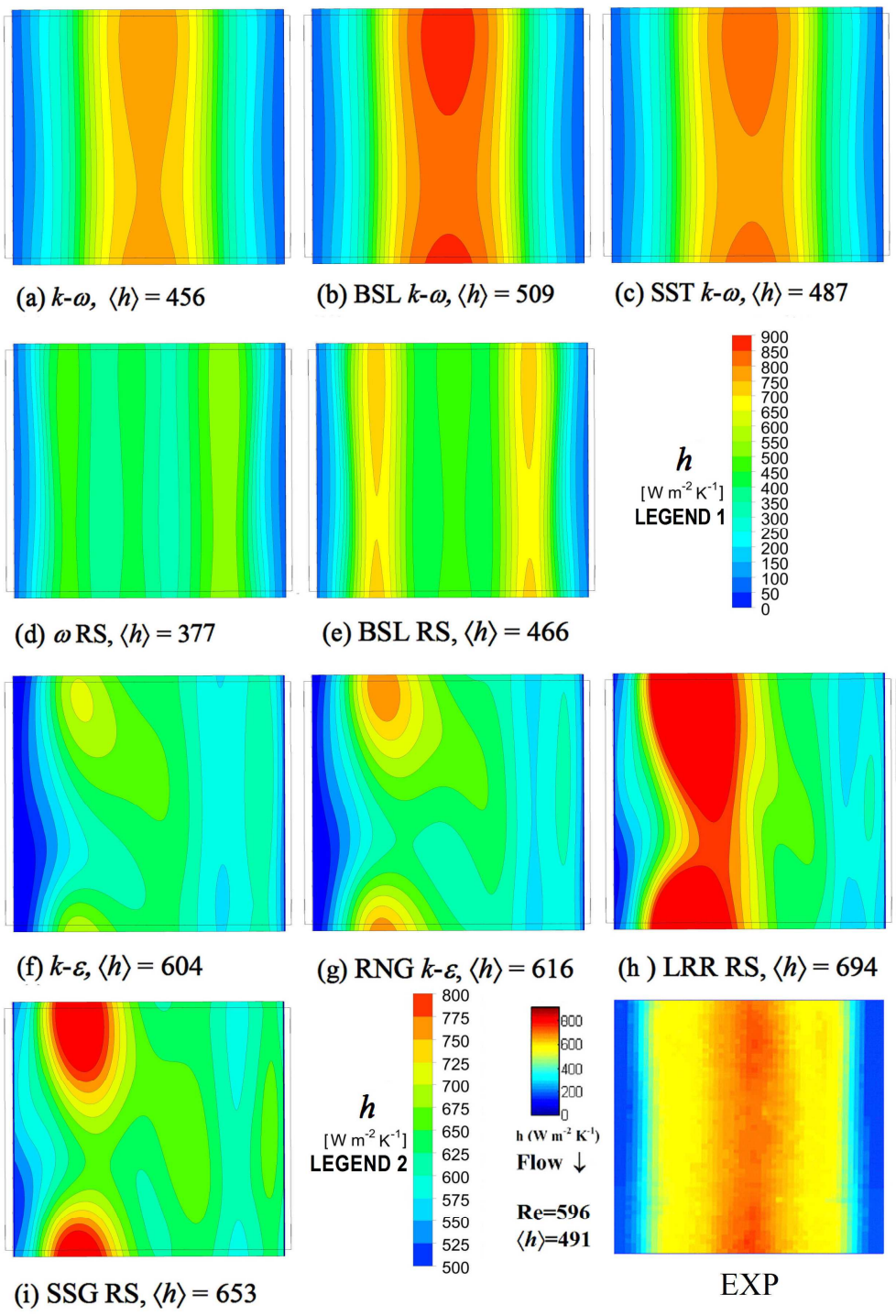

Figure 7. Distributions of the local heat transfer coefficient h on the top (thermally active) wall predicted by alternative turbulence models for Re=596 and a flow attack angle θ=0°. Surface-averaged values $\langle h \rangle$ are also reported. Legend 1 is for maps a-e (ω-based models), legend 2 for maps f-i (ε-based models). The corresponding experimental distribution is reported in the last map and exhibits an average value of 491 $Wm^{-2}K^{-1}$.

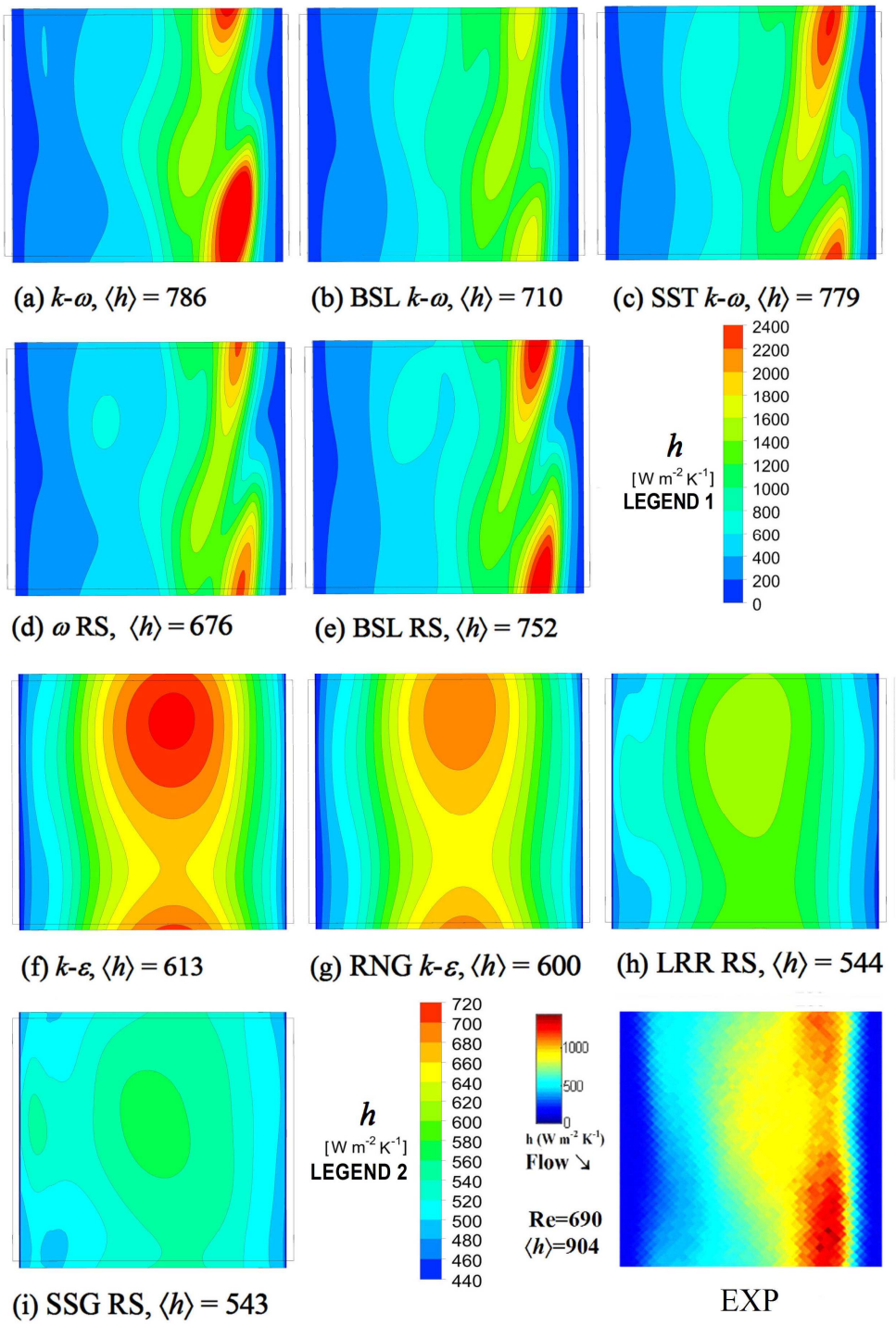

Figure 8. Distributions of the local heat transfer coefficient h on the top (thermally active) wall predicted by alternative turbulence models for Re=690 and a flow attack angle θ=45°. Surface-averaged values $\langle h \rangle$ are also reported. Legend 1 is for maps a-e (ω-based models), legend 2 for maps f-i (ε-based models). The corresponding experimental distribution is reported in the last map and exhibits an average value of 904 $Wm^{-2}K^{-1}$.

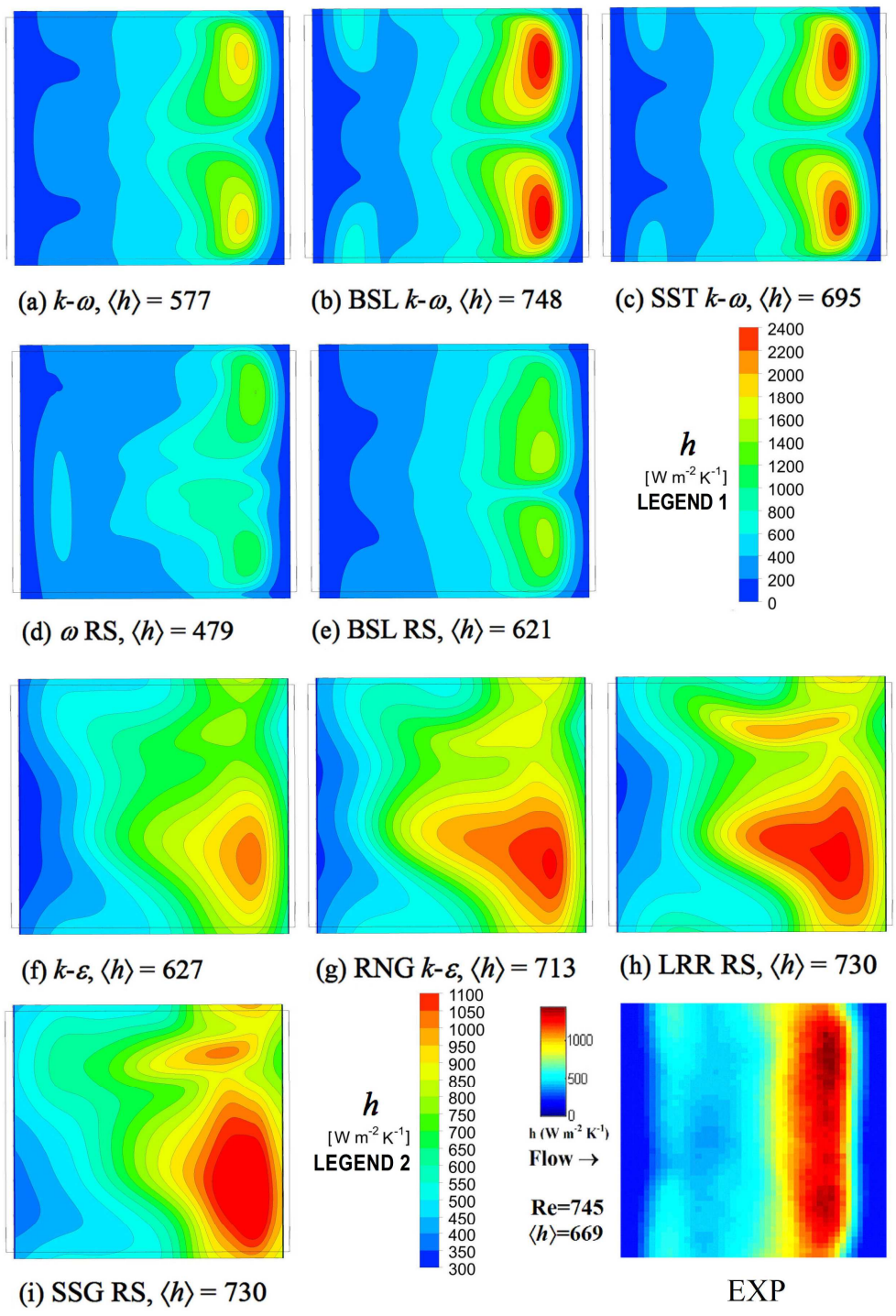

Figure 9. Distributions of the local heat transfer coefficient h on the top (thermally active) wall predicted by alternative turbulence models for Re=745 and a flow attack angle θ=90°. Surface-averaged values $\langle h \rangle$ are also reported. Legend 1 is for maps a-e (ω-based models), legend 2 for maps f-i (ε-based models). The corresponding experimental distribution is reported in the last map and exhibits an average value of 669 $Wm^{-2}K^{-1}$.

The following figures 10 to 12 concern test cases at higher Reynolds number (~1800). They are organized as figures 7-9 and regard the same three flow attack angles (θ=0°, 45° and θ=90°, respectively). The corresponding experimental distributions of h were shown in figure 6 (a-c) and are repeated for ease of comparison in the last map of each figure.

For θ=0° and Re=1840, figure 10, first-order ω-based models (a-c) yield acceptable results, with mean values of h overpredicted by ~10-15%. The least discrepancy on $\langle h \rangle$ is provided by the SST model (c), while the most symmetric distribution is provided by the k-ω model (a). The second-order ω-based models ω-RS and BSL-RS, maps (d) and (e), yield a larger overprediction of $\langle h \rangle$ and a multi-modal distributions of h along the spanwise direction which, although vaguely reminiscent of the multi-modal distribution exhibited by the experiments, is asymmetric with respect to the main flow direction and shows wrongly located and excessively high maxima. The ε-based models (f)-(i) all yield a strong overprediction of $\langle h \rangle$ (60-75%) and distributions which are strongly asymmetric with respect to the main flow direction.

For θ=45° and Re=1850, figure 11, ω-based models provide an acceptable agreement with the experiments both in the mean value and in the distribution of h. Values of $\langle h \rangle$ are underpredicted by 5 to 13%, the best agreement being provided, as in most other cases, by the SST model. The ε-based models using wall functions, graphs (f) to (i), yield unrealistically flat h distributions and a large underprediction of $\langle h \rangle$ (20-30%).

Finally, for θ=90° and Re=1820, figure 12, only the k-ω model (a) provides both the expected symmetry in the distribution of h and an acceptable agreement of $\langle h \rangle$ with the experimental result (7% overprediction). The other two first order ω-based models BSL k-ω and SST k-ω, maps (b) and (c), and much more so the second-order ω-based models ω RS and BSL RS, maps (d) and (e), yield asymmetric distributions of h although mean values $\langle h \rangle$ are still acceptable. The ε-based models using wall functions, maps (f) to (i), provide strongly asymmetric and irregular distributions of h and a large (25-40%) overprediction of $\langle h \rangle$.

Note that the experiments indicate that the orientation θ=45° provides the highest $\langle h \rangle$, whereas ε-based models predict that it provides the lowest. Note also that, at the present Reynolds numbers, all ε-based models, with the exception of the simple k-ε, encountered convergence difficulties and provided oscillatory solutions (the results shown in figures 10-12 and in table 5 are averages of these oscillatory solutions).

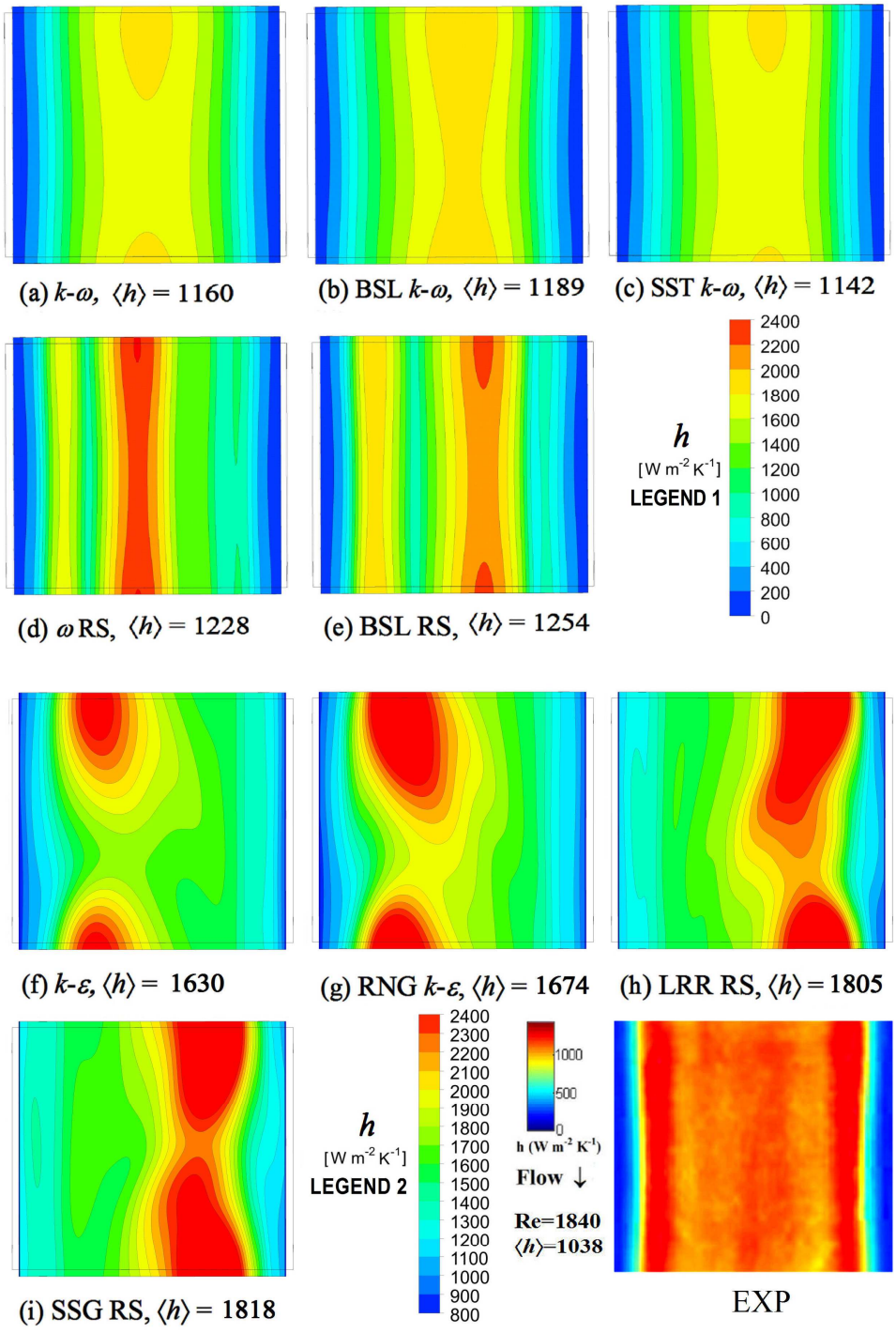

Figure 10. Distributions of the local heat transfer coefficient h on the top (thermally active) wall predicted by alternative turbulence models for Re=1840 and a flow attack angle θ=0°. Surface-averaged values $\langle h \rangle$ are also reported. Legend 1 is for maps a-e (ω-based models), legend 2 for maps f-i (ε-based models). The corresponding experimental distribution is reported in the last map and exhibits an average value of 1038 $Wm^{-2}K^{-1}$.

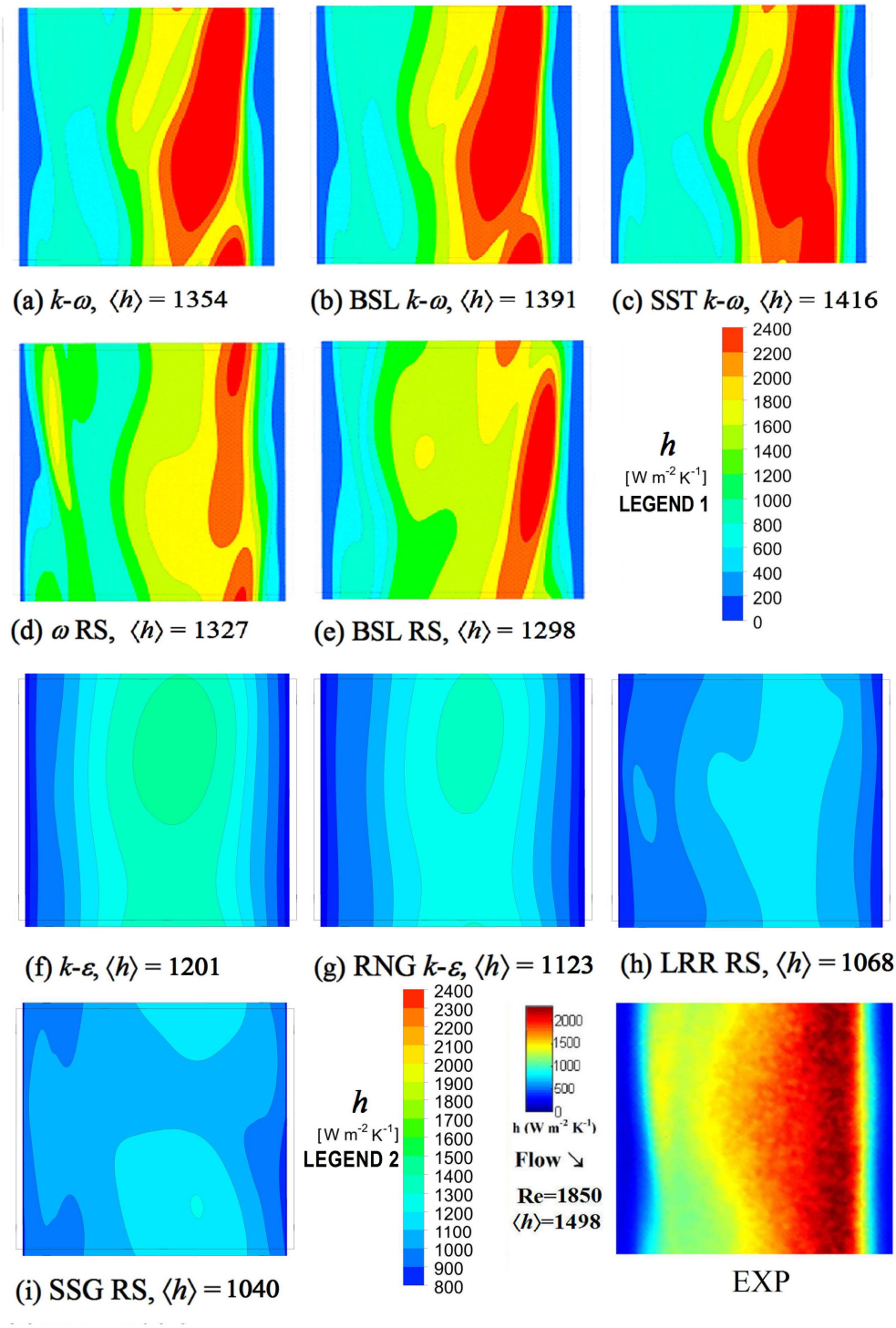

Figure 11. Distributions of the local heat transfer coefficient h on the top (thermally active) wall predicted by alternative turbulence models for Re=1850 and a flow attack angle θ=45°. Surface-averaged values $\langle h \rangle$ are also reported. Legend 1 is for maps a-e (ω-based models), legend 2 for maps f-i (ε-based models). The corresponding experimental distribution is reported in the last map and exhibits an average value of 1498 $Wm^{-2}K^{-1}$.

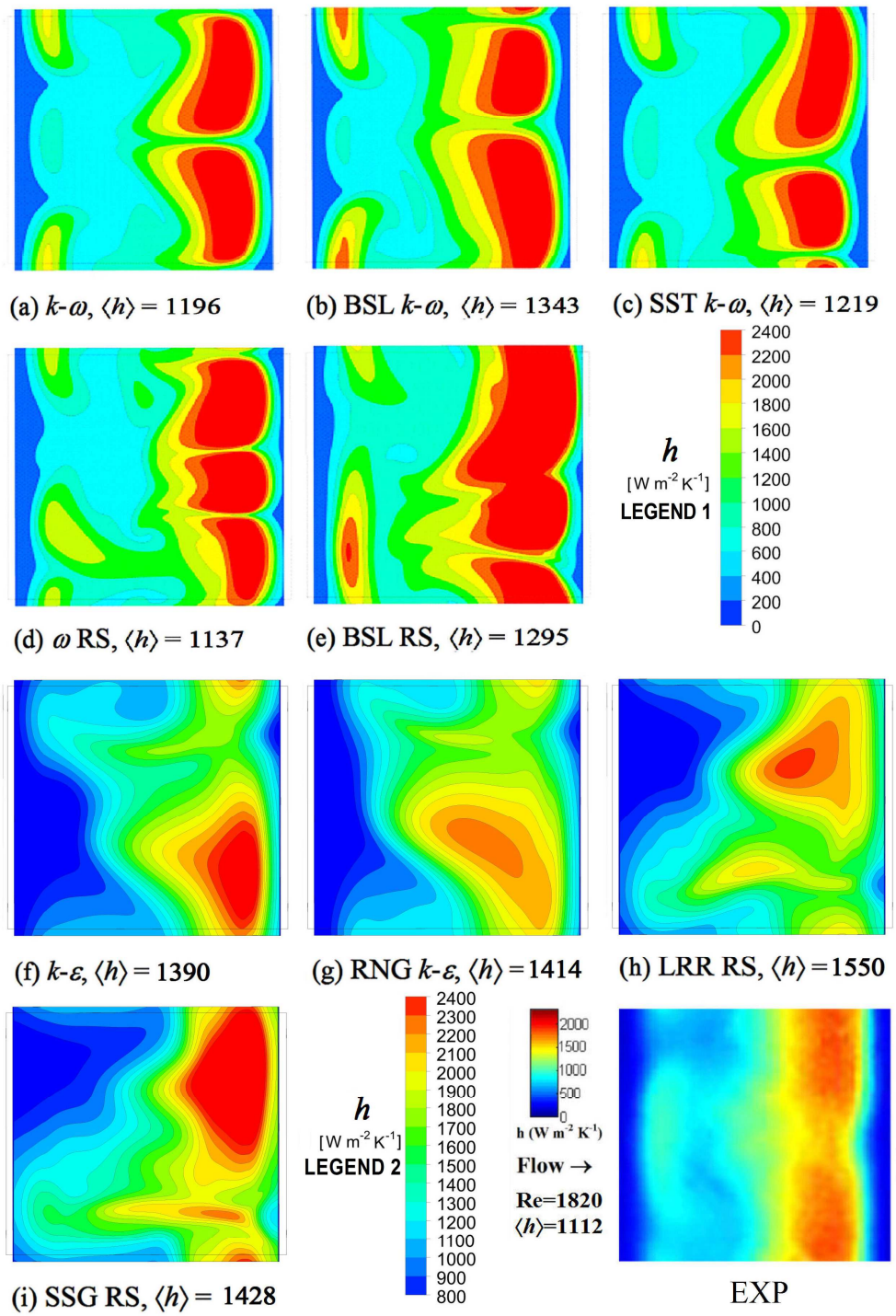

Figure 12. Distributions of the local heat transfer coefficient h on the top (thermally active) wall predicted by alternative turbulence models for Re=1820 and a flow attack angle θ=90°. Surface-averaged values $\langle h \rangle$ are also reported. Legend 1 is for maps a-e (ω-based models), legend 2 for maps f-i (ε-based models). The corresponding experimental distribution is reported in the last map and exhibits an average value of 1112 $Wm^{-2}K^{-1}$.

Figure 13 compares experimental and computational values of the surface-averaged heat transfer coefficient $\langle h \rangle$ on the top (thermally active) wall in the range Re=100~2000 for all three attack angles (0, 45 and 90°). Computational results were all obtained by the SST k-ω turbulence model. Circles denote the test cases for which experimental and predicted h distributions have been reported above. For the lowest Reynolds number cases (Re<~400), the SST model predicted laminarization and yielded results practically identical to those obtained by steady-state, laminar flow simulations (no turbulence model). This is in agreement with the experimental visual observations mentioned in Section 3.

At all flow attack angles, predictions are satisfactory up to Re≈500. For larger Re, a substantial underprediction is obtained for θ=45°, while results for θ=0° and 90° are generally overpredicted, especially at Re>1000.

On the whole, the influence of the flow attack angle is underpredicted; for example, at Re=1000 experimental results show that <h> increases from ~760 to ~1150, i.e. by ~50%, when θ increases from 0° to 45°, whereas CFD results indicate only a ~30% increase (from ~760 to ~1000).

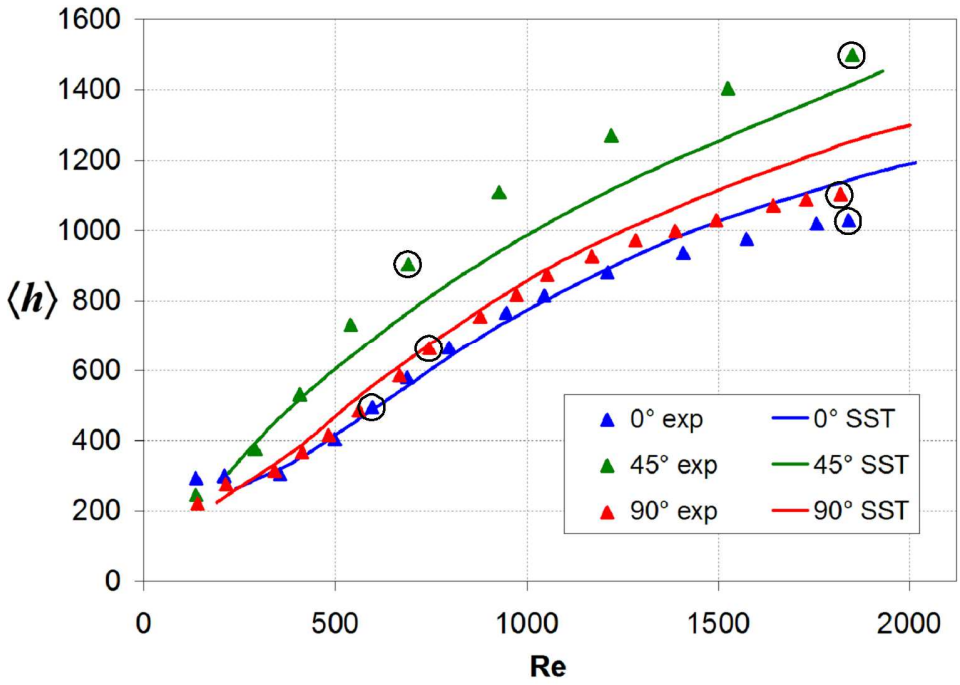

Figure 13. Comparison of experimental and computational (SST k-ω model) values of the surface-averaged heat transfer coefficient $\langle h \rangle$ (in $Wm^{-2}K^{-1}$) on the top (thermally active) wall for Re≈100-2000 and all three attack angles. Circles indicate the test cases for which h distributions were reported.

6 Conclusions

The main objective of the present paper was to identify turbulence models suitable for low-Reynolds number turbulent flows of the kind expected in spacer-filled channels typical of membrane processes, and, in particular, of membrane distillation. Therefore, the attention was focussed on each model's performance in terms of heat transfer, meaning both the distribution of the heat transfer coefficient h over a thermally active wall and the surface-averaged value $\langle h \rangle$ of this quantity. Experimental h maps, obtained by Liquid Crystal Thermography in scale models of membrane distillation modules, were used as a benchmark. Computational results were obtained by using a unit cell approach and a finite volume method, in conjunction with alternative turbulence models.

The comparison showed that, on the whole, most ω-based models (of either first or second order) which explicitly resolve the viscous / conductive sublayer qualitatively reproduced the overall distribution of h, while k-based models making use of wall functions (including again both first- and second-order, i.e. Reynolds Stress, models), at least in the form in which they are implemented in the Ansys-CFX code and for the present low Reynolds number turbulent flow conditions, yielded flat and unphysical h distributions. Also surface-averaged values $\langle h \rangle$ were better predicted by ω-based than by k-based models, which, in most cases, gave either strong underpredictions or comparably strong overpredictions.

Among ω-based models, second order ones (namely, ω Reynolds Stress and BSL Reynolds Stress) predicted in some cases unphysical h distributions, with multiple spanwise relative maxima or minima, for a flow attack angle θ of 0° (flow parallel to the rods touching the thermally active wall). They also yielded h distributions asymmetric with respect to the flow direction for θ=90° (flow orthogonal to the rods touching the thermally active wall), especially at high Reynolds numbers (1820-1850). First order ω-based models (k-ω, BSL k-ω, SST k-ω) gave more correct and physically consistent predictions of h average values and distributions both at moderate Re (~600-750) and at higher Re (1820-1850). In particular, the SST k-ω model provided the most satisfactory agreement of $\langle h \rangle$ with experimental results in all cases examined (max. 14% underprediction for moderate Re and θ=45°, max. 13% overprediction for high Re and θ=0° or 90°). The simpler k-ω model provided distributions with no unphysical asymmetry over the whole range of conditions examined, at the cost of an only slightly worse agreement with the experimental values of $\langle h \rangle$.

Finally, we would like to stress once again that, in the numerical simulations, periodicity (and not symmetry) boundary conditions were imposed at the side boundaries of the computational domain, in order to simulate the spatially repetitive features of the spacer lattice in the experimental facility (and in real MD units). In the experiments, for the orientations θ=0° (flow parallel to the upper spacer wires touching the upper, thermally active, wall) and θ =90° (flow orthogonal to these wires), wall temperature distributions symmetric with respect to the flow direction were always observed. In the simulations, this symmetry was approximately provided only by ω-based models featuring a fine resolution of the near-wall layer, whereas it was completely lost using ε-based models making use of wall functions. Therefore, it appears that, independent of the quantitative agreement of predicted h levels with experimental data, a full resolution of the near-wall layer is necessary in order correctly to predict the experimental symmetries.

Nomenclature

Symbol	*Quantity*	*Unit*
c_p	Specific heat at constant pressure	J kg^{-1} K^{-1}
H	Channel thickness	m
h	Local heat transfer coefficient	W m^{-2} K^{-1}
k	Turbulence kinetic energy	m^2 s^{-2}
P	Spacer pitch	m
Q	Volume flow rate	m^3 s^{-1}
$q"_w$	Wall heat flux	W m^{-2}
Re	Bulk Reynolds number	-
r	Thermal resistance	m^2 K W^{-1}
$S(h:x_i)$	Sensitivity of h to quantity x_i	-
s	Thickness	m
T	Temperature	K
U	Superficial velocity	m s^{-1}
u_i	i-th velocity component	m s^{-1}
W	Channel's spanwise extent	m

Greek symbols

ε	Turbulence dissipation rate	$m^2 s^{-3}$
θ	Flow attack angle	deg
λ	Thermal conductivity	$W m^{-1} K^{-1}$
μ	Viscosity	Pa s
ν	Kinematic viscosity	$m^2 s^{-1}$
ρ	Density	$kg m^{-3}$
σ	Uncertainty	[various]
ω	Turbulence frequency	s^{-1}

Subscripts

b	Bulk
c	Cold (external) temperature
PC	Polycarbonate
TLC	Thermochromic Liquid Crystals
w	Wall

References

[1] A. Campione, L. Gurreri, M. Ciofalo, G. Micale, A. Tamburini, A. Cipollina, Electrodialysis for water desalination: a critical assessment of recent developments on process fundamentals, models and applications, *Desalination* **434** (2018) 121-160.

[2] P. Onsekizoglu, Membrane Distillation: principle, advances, limitations and future prospects in food industry, in S. Zereshki (Editor), *Distillation - Advances from Modeling to Applications*, InTech (2012).

[3] I. Hitsov, T. Maere, K. DeSitter, C. Dotremont, I. Nopens, Modelling approaches in Membrane Distillation: a critical review, *Sep. Purif. Technol.* **142** (2015) 48–64.

[4] G. A. Fimbres-Weihs, D. E. Wiley, Review of 3D CFD modeling of flow and mass transfer in narrow spacer-filled channels in membrane modules, *Chem. Eng. Proc.* **49** (2010) 759–781.

[5] A. J. Karabelas, M. Kostoglou, C. P. Koutsou, Modeling of spiral wound membrane desalination modules and plants: review and research priorities, *Desalination* **356** (2015) 165–186.

[6] M. La Cerva, M. Ciofalo, L. Gurreri, A. Tamburini, A. Cipollina, G. Micale, On some issues in the computational modelling of spacer-filled channels for membrane distillation, *Desalination* **411** (2017) 101-111.

[7] A. R. Da Costa, A. G. Fane, D. E. Wiley, Spacer characterization and pressure drop modelling in spacer filled channel for ultrafiltration, *J. Membr. Sci.* **87** (1994) 79-98.

[8] M. Shakaib, S. M. F. Hasani, I. Ahmed, R. M. Yunus, A CFD study on the effect of spacer orientation on temperature polarization in Membrane Distillation modules, *Desalination* **284** (2012) 332–340.

[9] M. Shakaib, M. Ehtesham-ulHaq, I. Ahmed, R. M. Yunus, Modeling the effect of spacer orientation on heat transfer in Membrane Distillation, *World Academy of Science, Engineering and Technology* **72** (2010) 279–282.

[10] A. Tamburini, M. Renda, A. Cipollina, G. Micale, M. Ciofalo, Investigation of heat transfer in spacer-filled channels by experiments and direct numerical simulations, *Int. J. Heat Mass Transfer* **93** (2016) 1190-1205.

[11] J. A. Stasiek, M. W. Collins, M. Ciofalo, P. E. Chew, Investigation of Flow and Heat Transfer in Corrugated Passages – I. Experimental Results, *Int. J. Heat Mass Transfer* **39** (1996) 149-164.

[12] M. Ciofalo, I. Di Piazza, J. A. Stasiek, Investigation of flow and heat transfer in corrugated-undulated plate heat exchangers, *Heat and Mass Transfer* **36** (2000) 449-462.

[13] V. U. Kakade, G. D. Lock, M. Wilson, J. M. Owen, J. E. Mayhew, Accurate heat transfer measurements using Thermochromic Liquid Crystals. Part 2: Application to a rotating disc, *Int. J. Heat Fluid Flow* **30** (2009) 950–959.

[14] W. J. Hiller, S. Koch, T. A. Kowalewski, Three-dimensional structures in laminar natural convection in a cubic enclosure, *Exp. Thermal and Fluid Sci.* **2** (1989) 34-44.

[15] M. Ciofalo, M. Signorino, M. Simiano, Tomographic particle-image velocimetry and thermography in Rayleigh-Bénard convection using suspended Thermochromic Liquid Crystals and digital image processing, *Experiments in Fluids* **34** (2003) 156-172.

[16] A. Tamburini, P. Pitò, A. Cipollina, G. Micale and M. Ciofalo, A Thermochromic Liquid Crystals Image Analysis technique to investigate temperature polarization in spacer-filled channels for membrane distillation, *J. Membr. Sci.* **447** (2013) 260-273.

[17] H. T. Chen, H. C. Tseng, S. W. Jhu, J. R. Chang, Numerical and experimental study of mixed convection heat transfer and fluid flow characteristics of plate-fin heat sinks, *Int. J. Heat Mass Transfer* **111** (2017) 1050-1062.

[18] R. J. Moffat, Describing the uncertainties in experimental results, *Exp. Therm. Fluid Sci.* **1** (1988) 3-17.

[19] Ansys Inc., Ansys-CFX Reference Guide, Release 18.0 (2017).

[20] B. E. Launder, D. B. Spalding, The numerical computation of turbulent flows, *Comp. Meth. Appl. Mech. Eng.* **3** (1974) 269-289.

[21] V. Yakhot, S. A. Orszag, S. Thangam, T. B. Gatski, C. G. Speziale, Development of turbulence models for shear flows by a double expansion technique, *Phys. Fluids A* **4** (1992) 1510-1520.

[22] D. C. Wilcox, Reassessment of the scale-determining equation for advanced turbulence models, *AIAA Journal* **26** (1988) 1299-1310.

[23] F. R. Menter, Two-equation eddy-viscosity turbulence models for engineering applications, AIAA Journal **32** (1994) 1598-1605.

[24] F. R. Menter, M. Kuntz, R. Langtry, Ten years of industrial experience with the SST turbulence model, in *Turbulence, Heat and Mass Transfer 4*, K. Hanjaliç, Y. Nagano and M. Tummers, eds., Begell House, Inc., 2003.

[25] B. E. Launder, G. J. Reece, W. Rodi, Progress in the development of a Reynolds-stress turbulence closure, *J. Fluid Mechanics* **68** (1975) 537-566.

[26] C. G. Speziale, S. Sarkar, T. B. Gatski, Modelling the pressure-strain correlation of turbulence: an invariant dynamical systems approach, *J. Fluid Mechanics* **277** (1991) 245-272.